coatings

MDPI

Article

Growth without Postannealing of Monoclinic VO_2 Thin Film by Atomic Layer Deposition Using VCl_4 as Precursor

Wen-Jen Lee * and Yong-Han Chang

Department of Applied Physics, National Pingtung University, Pingtung 90003, Taiwan; crocodile710280@gmail.com

* Correspondence: wenjenlee@mail.nptu.edu.tw; Tel.: +886-8-7663800

Received: 18 October 2018; Accepted: 26 November 2018; Published: 27 November 2018

Abstract: Vanadium dioxide (VO_2) is a multifunctional material with semiconductor-to-metal transition (SMT) property. Organic vanadium compounds are usually employed as ALD precursors to grow VO_2 films. However, the as-deposited films are reported to have amorphous structure with no significant SMT property, therefore a postannealing process is necessary for converting the amorphous VO_2 to crystalline VO_2. In this study, an inorganic vanadium tetrachloride (VCl_4) is used as an ALD precursor for the first time to grow VO_2 films. The VO_2 film is directly crystallized and grown on the substrate without any postannealing process. The VO_2 film displays significant SMT behavior, which is verified by temperature-dependent Raman spectrometer and four-point-probing system. The results demonstrate that the VCl_4 is suitably employed as a new ALD precursor to grow crystallized VO_2 films. It can be reasonably imagined that the VCl_4 can also be used to grow various directly crystallized vanadium oxides by controlling the ALD-process parameters.

Keywords: vanadium dioxide; atomic layer deposition; vanadium oxide; vanadium tetrachloride; semiconductor-to-metal transition

1. Introduction

Vanadium dioxide (VO_2) has attracted extensive research interest during the past decades owing to its unique behavior, called semiconductor-to-metal transition (SMT) or insulator-to-metal transition (IMT), which accompanies the reversible and ultrafast phase transition between monoclinic VO_2 [VO_2(M)] and tetragonal rutile VO_2 [VO_2(R)] at temperatures around 340 K (~67 °C) [1–5]. Thus, the optical and electrical properties of VO_2 can be switched by controlling the SMT behavior of VO_2 [6,7]. Numerous factors for adjusting the SMT behavior of VO_2 have already been established that include impurity doping [8], stoichiometry [9], strain [10], grain boundary [11], oxygen vacancy [12], applied external electrical field [13], and light irradiation [14]. Therefore, the VO_2 has been widely investigated as a key material for applications in the smart thermochromic windows [15], two-terminal electronic devices [16], electric-field-effect three-terminal devices [17,18], integrated optical circuits [19], electronic oscillators [20], metamaterials [21], memristive devices [22], programmable critical thermal sensors [23], gas sensors [24], and so forth.

Various techniques had been employed for preparing VO_2 films, including the sol–gel method [22,23], electron-beam evaporation [25,26], sputtering [5,17], pulsed laser deposition (PLD) [27,28], molecular beam epitaxy (MBE) [16,29], chemical vapor deposition (CVD) [30–34], and atomic layer deposition (ALD) [35–50]. Among them, ALD is an excellent technique which has drawn much attention due to its many advantages, including preparation of the highly conformal thin films with almost 100% step coverage, accurate control of film thickness at the atomic scale,

low growth temperature, and wide-area uniformity. These features make ALD a powerful technique for the fabrication of emerging nanostructures and nanodevices [51–53].

Generally, organic vanadium compounds are employed as ALD precursors and reacted with H_2O or O_3 to grow vanadium oxide thin films, such as tetrakis(ethylmethylamino)vanadium (TEMAV) [35–42], vanadyl isopropoxide (VTIP) [43–46], and vanadyl triisopropoxide (VTOP) [47–50]. However, the organic precursors (TEMAV, VTIP, and VTOP) are only suitable for low process temperatures in ALD because the decomposition temperatures of TEMAV, VTIP, and VTOP are about 175 [35,40], 200 [43], and 180 °C [49,50], respectively. When the process temperature is higher than the decomposition temperature of the precursor, the growth mechanism of film will be changed from ALD to CVD-like mode [35,40,43,49,50]. In this case, the film is grown by CVD instead of ALD. This is why the low temperature of 120–170 °C is usually used for the film growth of ALD using TEMAV, VTIP, or VTOP as precursor. However, the low process temperature is not enough to grow crystalline films. Therefore, the as-deposited vanadium oxide films grown by ALD from organic vanadium precursors are generally reported to have amorphous structures with no significant SMT behavior and a postannealing process is necessary for converting the amorphous to crystalline VO_2. Previous studies have reported that postannealing in N_2, He, O_2, or N_2/O_2 mixed gas with a low O_2 partial pressure resulted in crystalline monoclinic VO_2 for the temperature range of 425–585 °C [35–42]. Since the extra postannealing process is necessary to obtain a crystalline VO_2, it results in higher manufacturing costs and increases the failure possibilities of the process and products.

This work reports that a directly crystalline VO_2 film has been successfully grown by ALD using vanadium tetrachloride (VCl_4) and H_2O as precursors at a reaction temperature of 350 °C without any postannealing process. It is noticed that the inorganic VCl_4 is used as an ALD precursor for the first time, although a few papers reported that the VCl_4 had been used in traditional chemical vapor deposition (CVD) techniques [30–32]. The VO_2 film has a significant SMT behavior with a VO_2(M)-to-VO_2(R) phase-transition temperature of about 61 ± 1 °C, which is verified from temperature-dependent Raman spectra and sheet-resistance variations of VO_2 film. Besides, the VO_2 film exhibits two orders of magnitude change in sheet resistance across the semiconductor-to-metal transition although the film thickness is only 30 nm. The results demonstrated that crystalline VO_2 films can be directly grown by ALD using VCl_4 and H_2O as precursors without any postannealing process, presenting a new selection of precursors for the ALD process to grow the crystalline VO_2 films.

2. Materials and Methods

In this work, VO_2 films were grown on native silicon-oxide-covered Si (100) substrates by ALD at 350 °C with 1000 reaction cycles. VCl_4 and H_2O were employed as precursors to grow the VO_2 films, and Ar was used as purge gas. The reservoirs of the VCl_4 and H_2O precursors were kept at the temperatures of 30 and 25 °C, respectively. The dosing rates of VCl_4 and H_2O were 0.288 and 0.296 cc/pulse, respectively, as determined by the reservoir temperature and vapor injection time. The flow rate of Ar was 5 sccm, as controlled by a mass flow controller (MFC, SEC-4400M, HORIBA STEC, Kyoto, Japan). An eight-step sequence of gas injection was applied in an ALD cycle, as combined four conventional gas-injection steps and four additional pump-down steps. The pump-down steps can effectively evacuate excess precursors and byproducts to obtain high-quality films with low Cl impurity contents and ensure the achievement of "true ALD mode" growth [54,55]. The time for each step in an ALD cycle was 0.1, 1, 0.5, 1, 0.5, 1, 0.5, and 1 s for VCl_4 vapor injection, pump-down, Ar purge, pump-down, H_2O vapor injection, pump-down, Ar purge, and pump-down, respectively.

The crystalline structures of the VO_2 films were examined by an X-ray diffractometer (XRD, D8 Advance Eco, Bruker, Karlsruhe, Germany) at 30 and 90 °C. The surface morphologies of the film were observed with a high-resolution scanning electron microscope (SEM, SU8000, Hitachi, Tokyo, Japan). In addition, in order to obtain real surface morphology of the film, the SEM analysis was performed without any conductive coating on the VO_2 film surface. The cross-sectional microstructures of the VO_2

films were observed by a high-resolution transmission electron microscope (TEM, JEM-2100F, JEOL, Tokyo, Japan). The film thickness was measured from the cross-sectional TEM micrograph and the growth rate of the VO_2 film was estimated from an equation of "growth rate = (film thickness/numbers of ALD cycles)". The chemical composition of the VO_2 film was analyzed by a high-resolution X-ray photoelectron spectrometer (XPS, Quantera SXM, ULVAC-PHI, Chigasaki, Japan). In addition, the XPS analysis was performed on the VO_2 film surface before and after Ar ion etching with an etching depth of about 2 nm. The temperature-dependent Raman spectra of the VO_2 film were examined at temperatures between 30 and 80 °C by a micro Raman spectrometer (Raman, UniRAM II, Uninanotech, Yongin, Korea) with a temperature-controllable sample stage. The temperature-dependent sheet resistance of the VO_2 film was measured at temperatures between 30 and 90 °C by a Keithley 2614B SourceMeter (Keithley, Solon, OH, USA) under a four-point probing configuration with a temperature-controllable sample stage.

3. Results and Discussion

Figure 1 shows the XRD patterns of VO_2 film measured at 30 and 90 °C, which demonstrate the structural transition of VO_2 film from monoclinic (30 °C) to tetragonal rutile (90 °C) phase. The VO_2 film measured at 30 °C (Figure 1a) displays that two XRD peaks located at 2θ of 27.9° and 55.4° can be indexed to the (011) and (220) planes of monoclinic VO_2(M) (JCPDS no.: 82–0661), respectively. When the temperature is raised to 90 °C (Figure 1b), two XRD peaks located at 2θ of 27.6° and 55.4° are detected, which can be assigned to the (110) and (211) planes of tetragonal rutile VO_2(R) (JCPDS no.: 79–1655), respectively. In addition, because the VO_2 film is grown on Si substrate, an obvious XRD peak of Si (113) at 2θ of 51.9° has also been detected (Supplementary materials: Part 1). Figure 1c is a comparison of Figure 1a,b, which clearly shows an XRD peak shift of VO_2(M) (011) to VO_2(R) (110) peak in $26° \leq 2θ \leq 30°$ and the XRD peak of Si substrate does not shift. The XRD peak-shifting behavior is a diagnostic feature for the phase transition of VO_2 film from monoclinic to tetragonal rutile structure. Previously, the similar XRD peak-shifting phenomenon had also been reported by Wu et al. [56] for confirming the phase transformation of monoclinic VO_2 to tetragonal rutile VO_2.

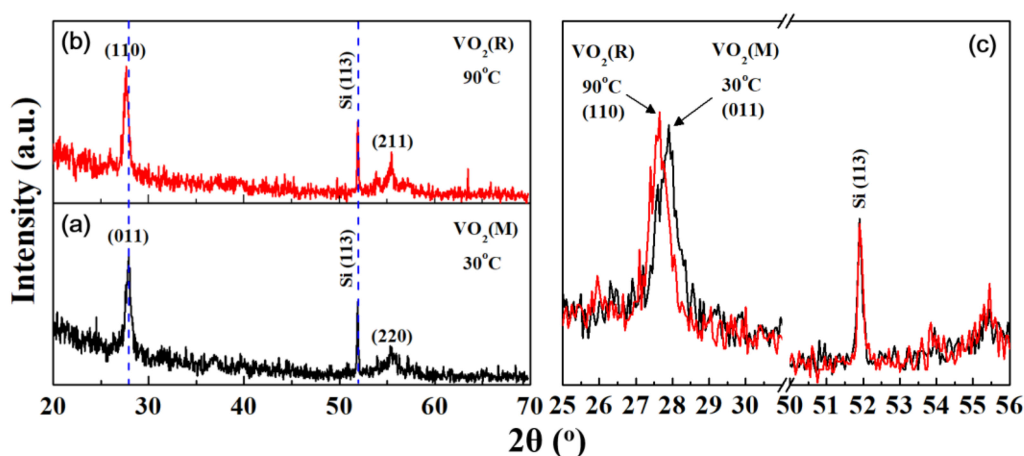

Figure 1. XRD patterns of VO_2 film measured at (**a**) 30 °C and (**b**) 90 °C. (**c**) A comparison of (**a**) and (**b**).

Figure 2 shows the SEM and TEM analyzed results for surface and cross-sectional microstructures of the VO_2 film, respectively. The SEM image of surface morphology of the VO_2 film (Figure 2a) displays a conformal VO_2 film with bigger grains surrounded by small grains; the grain sizes of big and small grains are about 78 ± 14 and 40 ± 6 nm, respectively. According to the cross-sectional TEM bright-field and dark-field images (Figure 2b,c), it can be clearly observed that the VO_2 film is grown on a native oxide layer (SiO_x) of Si substrate and constructed from columnar grains. The thickness of the VO_2 film is about 30 nm, and displays its growth rate at about 0.03 nm/cycle. Moreover, the VO_2

grains are directly crystallized and grown on the top surface of the native oxide layer, which is verified by the high-resolution TEM (HR-TEM) image of the $VO_2/SiO_x/Si$ interface (Figure 2d). The HR-TEM image also reveals a clear lattice fringe of about 0.32 nm, corresponding to the (011) plane of VO_2(M). The selected-area electron-beam diffraction (SA-EBD) pattern obtained by focusing the electron beam on an individual VO_2 grain is shown in Figure 2e; the SA-EBD pattern can be indexed to monoclinic VO_2(M) in agreement with the XRD results.

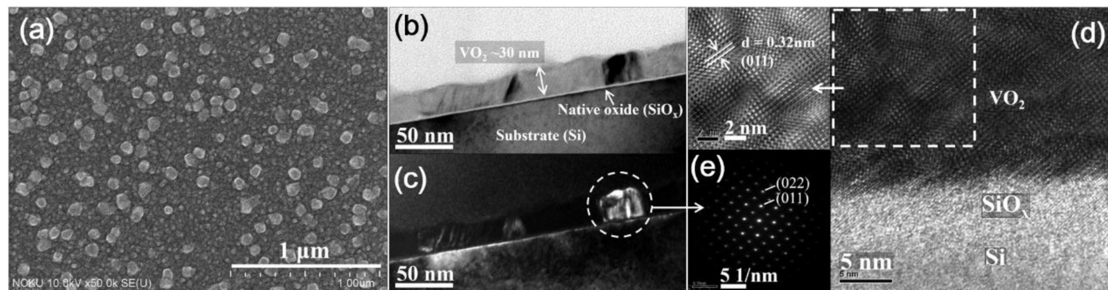

Figure 2. Microstructure analyses of VO_2 film. (**a**) An SEM top-view image. TEM cross-sectional (**b**) bright-field and (**c**) dark-field images. (**d**) A high-resolution TEM (HR-TEM) image of the $VO_2/SiO_x/Si$ interface. (**e**) The selected-area electron-beam diffraction (SA-EBD) pattern obtained by focusing the electron beam on an individual VO_2 grain.

Figure 3 shows the V2p, O1s, and Cl2p XPS spectra for original (before etching) and after argon-ion etching surface of VO_2 film. In addition, the chemical composition of VO_2 film calculated from XPS spectra are shown in Table 1. The V and O concentrations of VO_2 film are about 25.7 at.% and 74.3 at.%, respectively, for the film before surface etching and are about 33.1 at.% and 66.9 at.%, respectively, for the film after surface etching. The results clearly indicate that the original surface of the VO_2 film has a higher oxygen concentration because the VO_2 film was exposed to air (oxygen-rich) environment, resulting in absorption of oxygen and a native oxide layer (overoxidation layer) forming on the surface of the VO_2 film [26,33,34,39,41,43,57,58]. After argon-ion etching, surface contamination and the native oxide layer of the VO_2 film had been removed, and the atomic proportion of V:O atom was about 1:2 in agreement with the stoichiometry of VO_2. Besides, no Cl impurity had been detected in the VO_2 film, demonstrating the Cl concentration in the VO_2 film was lower than the detection limit of XPS (approximately 0.1 at.%). It is noteworthy that this work successfully achieved VO_2 film with high purity (Cl impurity <0.1 at.%) by using a low growth temperature of 350 °C, which can be attributed to the additional pump-down steps in the ALD reaction cycles effectively evacuating excess precursors and byproducts [54]. In a previous study, Cheng et al. reported that implementation of pump-down steps into the gaseous-pulse cycle of ALD can effectively reduce the Cl residues. They used $TiCl_4$ as ALD precursor to grow TiN films by using conventional four-step ALD and modified six-step ALD (adding two pump-down steps). Their results showed that the Cl residues of TiN films can be decreased from about 7.7 at.% to 2.3 at.% at the growth temperature of 300 °C [54].

In Figure 3a, the V2p3/2 peak of the original VO_2 film (before surface etching) can be fitted with two peaks at binding energy of about 517.2 and 515.6 eV, which can be assigned to V^{5+} and V^{4+}, respectively [26,33,34,39,41,43,57,58]. Musschoot et al. [43] and Sliversmit et al. [57] reported that the V^{5+} signal is mainly contributed from the native oxide layer (overoxidation layer) of VO_2 film. After surface etching (to remove the native oxide layer), the $V2p_{3/2}$ peak has a maximum at 515.6 eV (assigned to V^{4+}), which primarily confirms VO_2 stoichiometry. In Figure 3b, the O1s XPS peaks are located at binding energy of about 529.8 and 530.5 eV for the original and after-surface-etching VO_2 film, showing a peak-shifting phenomenon. The similar peak-shifting phenomenon of O1s XPS peak for VO_2 film after surface etching by argon ion sputtering had also been observed by Musschoot et al. [43].

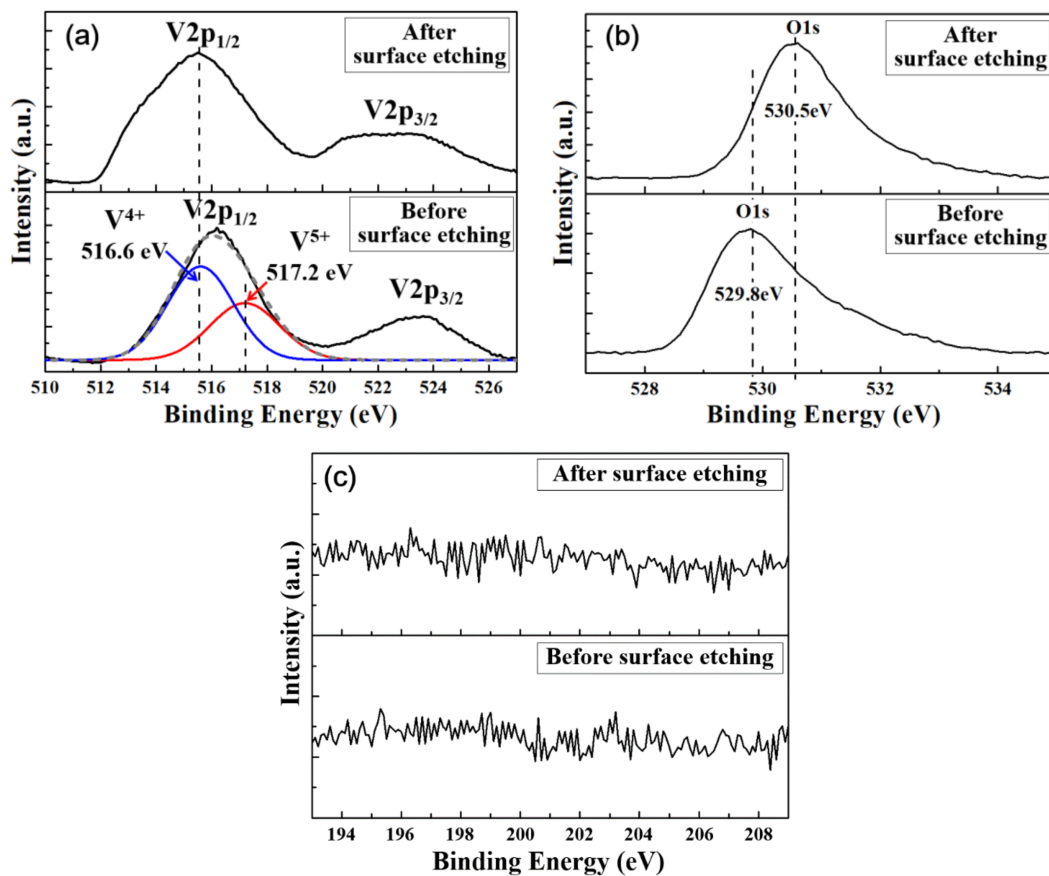

Figure 3. (**a**) V2p, (**b**) O1s, and (**c**) Cl2p XPS spectra for original (before etching) and after argon-ion etching surface of VO_2 film.

Table 1. Chemical composition of VO_2 thin film analyzed by XPS.

Elemental Content	Before Surface Etching	After Surface Etching
V (at.%)	25.7	33.1
O (at.%)	74.3	66.9
Cl (at.%)	<0.1	<0.1

Figure 4a,b show the selected temperature-dependent Raman spectra of the VO_2 film for heating and cooling cycles, respectively. It is noticed that the full temperature-dependent Raman spectra of the VO_2 films for temperatures between 30 and 80 °C in heating and cooling cycles are shown in Figures S1 and S2, respectively. As shown in Figure 4, four Raman peaks at 194, 224, 305, and 616 cm^{-1} are associated with the monoclinic phase VO_2 [25,26,59–61]. The peaks of 194, 305, and 616 cm^{-1} are assigned to A_g phonon vibration modes [25,26,59,60] and the peak of 224 cm^{-1} can be assigned to A_g + B_g mode [61]. The low-frequency phonons at 194 and 224 cm^{-1} relate to lattice motion involving V–V bonds, while the other peaks are attributed to V–O bonds [26,59–61]. Peaks located at 301, 520, and 935–990 cm^{-1} are contributed from the silicon substrate that compared with the Raman spectrum of the silicon substrate (Figure 5). Moreover, the phonon intensities of 194, 224, and 616 cm^{-1} gradually disappear as the temperature increases and display the reversibility during the cooling cycle. However, the peak intensity of 305 cm^{-1} does not show an evident change due to an overlap signal between 305 and 301 cm^{-1} for VO_2 and silicon substrate, respectively.

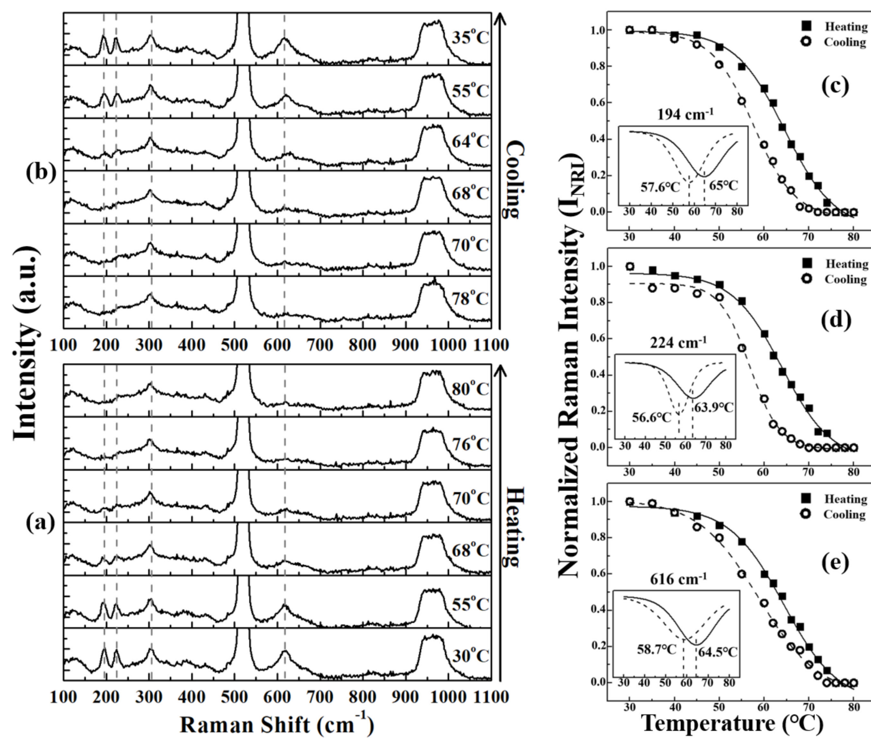

Figure 4. Temperature-dependent Raman spectra of the VO_2 film: (**a**) heating cycle, (**b**) cooling cycle, and relative Raman intensity of the A_g phonon mode at (**c**) 194, (**d**) 224, and (**e**) 616 cm^{-1}.

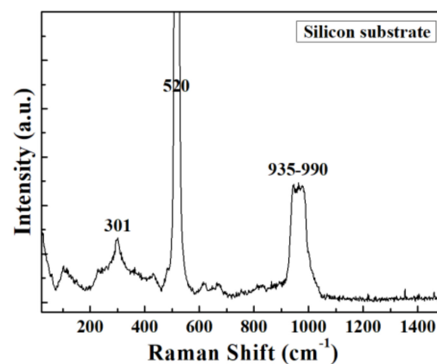

Figure 5. Raman spectrum of the silicon substrate.

Furthermore, the plots of normalized Raman intensity variations for the A_g phonon vibration mode at 194, 224, and 616 cm^{-1} are shown in Figure 4c,d,e, respectively. The normalized Raman intensity of VO_2 film was calculated from the equation below:

$$I_{\mathrm{NRI}} = \frac{I_T - I_{80}}{I_{30} - I_{80}} \quad (1)$$

where I_{NRI} is the normalized Raman intensity, I_T is the Raman intensity measured at indicated temperature (T), I_{30} and I_{80} are the Raman intensities measured at 30 and 80 °C, respectively. It can be seen clearly that the plots of Raman intensity vibrations show a hysteresis feature for Raman shift at 194, 224, and 616 cm^{-1}. The phase transition temperatures of VO_2 film estimated by the differential curves (as inserts) are about 65, 63.9, and 64.5 °C for 194, 224, and 616 cm^{-1} in the heating process, respectively. In the cooling process, the phase transition temperatures of VO_2 film are about 57.6, 56.6, and 58.7 °C for 194, 224, and 616 cm^{-1}, respectively. Therefore, the overall SMT temperatures

estimated from the middle of the hysteresis curves are about 61.3, 60.25, and 61.6 °C for 194, 224, and 616 cm^{-1}, respectively.

The temperature-dependent sheet-resistance (SR) variation of VO_2 film is shown in Figure 6, displaying a thermal hysteresis variation. Besides, the SR variation has approached two orders of magnitude across the semiconductor-to-metal transition (SMT) of the VO_2 film (SR changed from 2.2×10^4 to 2.7×10^2 Ω/□ for the temperature raised from 40 to 80 °C) so that the value of the resistance ratio agrees with the typical VO_2 film thickness less than 50 nm (typically, the resistance ratios of most VO_2 films across the SMT are in the range of 10^2–10^3 for thickness <50 nm) [29]. Furthermore, a sharp drop of SR can be clearly observed in the heating cycle, determining a phase transition temperature of about 63 °C, and a sharp rise of SR in the cooling cycle with a phase transition temperature of about 56 °C can be also seen in Figure 6. Therefore, the SMT temperature estimated from the middle of thermal hysteresis SR variation is about 60.0 °C.

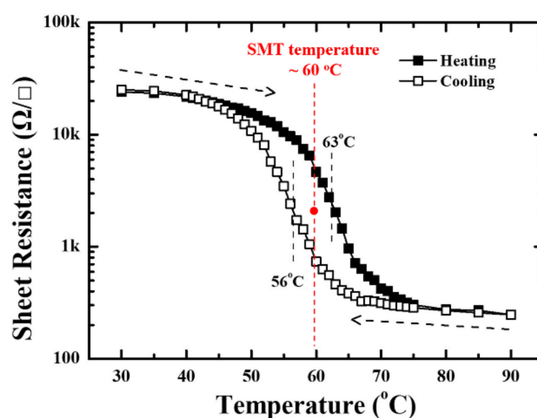

Figure 6. Temperature-dependent sheet-resistance variation of the VO_2 film.

There are several parameters that may affect the temperature-dependent electrical properties of VO_2, such as changes in impurity content, stoichiometry, strain, oxygen vacancies, and the presence of grain boundaries [8–12]. In this work, the SMT temperature of VO_2 film evaluated from the temperature-dependent Raman spectra and sheet-resistance variation is about 61 ± 1 °C, slightly different from the well-known 340K (~67 °C), which can be reasonably attributed to the influence of grain boundary density because the VO_2 film has a polycrystalline structure with considerable grain boundaries.

4. Conclusions

In conclusion, the VCl_4 is successfully employed as a new ALD precursor to grow a VO_2 film on the Si (100) substrate. Besides, without any postannealing process required, the as-deposited VO_2 film is directly crystallized and provides a significant SMT property. Moreover, it can be reasonably imagined that the VCl_4 can be used not only to grow crystalline VO_2 films, but also to grow other different vanadium oxides (VO_x, $x \neq 2$) by controlling the ALD-process parameters (such as process temperature, VCl_4/H_2O ratio, and so forth). It is just like this that the VCl_4 had been used as a precursor for atmospheric pressure CVD to grow different vanadium oxides (VO_2 and V_2O_5) by controlling process parameters of temperature and VCl_4/H_2O ratio [30–32]. We anticipate this work to be a starting point for using VCl_4 as a precursor to grow various directly crystallized vanadium oxides by ALD without any postannealing process.

Supplementary Materials: The following are available online at http://www.mdpi.com/2079-6412/8/12/431/s1, Part 1: A brief report provided by Bruker Corporation for explaining "Why Si (113) peak appears in GIXRD profile?" Part 2: Full temperature-dependent Raman spectra of the VO_2 films. Figure S1: Raman spectra of the VO_2 film measured at indicant temperature for heating cycle (temperature from 30 to 80 °C), Figure S2: Raman spectra of the VO_2 film measured at indicant temperature for cooling cycle (temperature from 78 to 35 °C).

Funding: This research was funded by the Ministry of Science and Technology of Taiwan (Nos.: MOST 105-2221-E-153-001 and MOST 106-2221-E-153-004).

Acknowledgments: The authors would like to thank Dr. Ya-Ching Yang (Bruker Corporation) for discussing and providing a brief report to explain "Why Si (113) peak appears in GIXRD profile?", Ms. Hui-Jung Shih (Instrument Center, NCKU) for HR-SEM analysis, Ms. Mei-Lan Liang and Ms. Shih-Wen Tseng (Center for Micro/Nano Science and Technology, NCKU) for FIB and TEM analyses, and Ms. Swee-Lan Cheah (Instrument Center, NTHU) for HR-XPS analysis.

Conflicts of Interest: The authors declare no conflict of interest.

References

1. Morin, F.J. Oxides which show a metal-to-insulator transition at the Neel temperature. *Phys. Rev. Lett.* **1959**, *3*, 34–36. [CrossRef]
2. Barker, A.S.; Verleur, H.W.; Guggenheim, H.J. Infrared optical properties of vanadium dioxide above and below the transition temperature. *Phys. Rev. Lett.* **1966**, *17*, 1286–1289. [CrossRef]
3. Park, J.H.; Coy, J.M.; Kasirga, T.S.; Huang, C.; Fei, Z.; Hunter, S.; Cobdem, D.H. Measurement of a solid-state triple point at the metal-insulator transition in VO_2. *Nature* **2013**, *500*, 431–434. [CrossRef] [PubMed]
4. O'Callahan, B.T.; Jones, A.C.; Park, J.H.; Cobden, D.H.; Atkin, J.M.; Raschke, M.B. Inhomogeneity of the ultrafast insulator-to-metal transition dynamics of VO_2. *Nat. Commun.* **2015**, *6*, 6849. [CrossRef] [PubMed]
5. Cueff, S.; Li, D.; Zhou, Y.; Wong, F.J.; Kurvits, J.A.; Ramanathan, S.; Zia, R. Dynamic control of light emission faster than the lifetime limit using VO_2 phase-change. *Nat. Commun.* **2015**, *6*, 8636. [CrossRef] [PubMed]
6. Yang, Z.; Ko, C.; Ramanathan, S. Oxide electronics utilizing ultrafast metal-insulator transitions. *Annu. Rev. Mater. Res.* **2011**, *41*, 337–367. [CrossRef]
7. Nakano, M.; Shibuya, K.; Okuyama, D.; Hatano, T.; Ono, S.; Kawasaki, M.; Iwasa, Y.; Tokura, Y. Collective bulk carrier delocalization driven by electrostatic surface charge accumulation. *Nature* **2012**, *487*, 459–462. [CrossRef] [PubMed]
8. Wang, N.; Liu, S.; Zeng, X.T.; Magdassi, S.; Long, Y. Mg/W-codoped vanadium dioxide thin films with enhanced visible transmittance and low phase transition temperature. *J. Mater. Chem. C* **2015**, *3*, 6771–6777. [CrossRef]
9. Zhang, S.; Kim, I.S.; Lauhon, L.J. Stoichiometry engineering of monoclinic to rutile phase transition in suspended single crystalline vanadium dioxide nanobeams. *Nano Lett.* **2011**, *11*, 1443–1447. [CrossRef] [PubMed]
10. Petraru, A.; Soni, R.; Kohlstedt, H. Voltage controlled biaxial strain in VO_2 films grown on $0.72Pb(Mg_{1/3}Nb_{2/3})$-$0.28PbTiO_3$ crystals and its effect on the transition temperature. *Appl. Phys. Lett.* **2014**, *105*, 092902. [CrossRef]
11. Jian, J.; Chen, A.; Zhang, W.; Wang, H. Sharp semiconductor-to-metal transition of VO_2 thin films on glass substrates. *J. Appl. Phys.* **2013**, *114*, 244301. [CrossRef]
12. Jeong, J.; Aetukuri, N.; Graf, T.; Schladt, T.D.; Samant, M.G.; Parkin, S.S.P. Suppression of metal-insulator transition in VO_2 by electric field-induced oxygen vacancy formation. *Science* **2013**, *339*, 1402–1405. [CrossRef] [PubMed]
13. Aetukuri, N.B.; Gary, A.X.; Drouard, M.; Cossale, M.; Gao, L.; Reid, A.H.; Kukreja, R.; Ohldag, H.; Jenkins, C.A.; Arenholz, E.; et al. Control of the metal–insulator transition in vanadium dioxide by modifying orbital occupancy. *Nat. Phys.* **2013**, *9*, 661–666. [CrossRef]
14. Wu, J.M.; Liou, L.B. Room temperature photo-induced phase transitions of VO_2 nanodevices. *J. Mater. Chem.* **2011**, *21*, 5499–5504. [CrossRef]
15. Xu, F.; Cao, X.; Luo, H.; Jin, P. Recent advances in VO_2-based thermochromic composites for smart windows. *J. Mater. Chem. C* **2018**, *6*, 1903–1919. [CrossRef]
16. Shukla, N.; Parihar, A.; Freeman, E.; Paik, H.; Stone, G.; Narayanan, V.; Wen, H.; Cai, Z.; Gopalan, V.; Engel-Herbert, R.; et al. Synchronized charge oscillations in correlated electron systems. *Sci. Rep.* **2014**, *4*, 4964. [CrossRef]
17. Ruzmetov, D.; Gopalakrishnan, G.; Ko, C.; Narayanamurti, V.; Ramanathan, S. Three-terminal field effect devices utilizing thin film vanadium oxide as the channel layer. *J. Appl. Phys.* **2010**, *107*, 114516. [CrossRef]
18. Yajima, T.; Nishimura, T.; Toriumi, A. Positive-bias gate-controlled metal–insulator transition in ultrathin VO_2 channels with TiO_2 gate dielectrics. *Nat. Commun.* **2015**, *6*, 10104. [CrossRef] [PubMed]

19. Briggs, R.M.; Pryce, I.M.; Atwater, H.A. Compact silicon photonic waveguide modulator based on the vanadium dioxide metal-insulator phase transition. *Opt. Express* **2010**, *18*, 11192–11201. [CrossRef] [PubMed]
20. Gu, Q.; Falk, A.; Wu, J.Q.; Ouyang, L.; Park, H. Current-driven phase oscillation and domain-wall propagation in $W_xV_{1-x}O_2$ nanobeams. *Nano Lett.* **2007**, *7*, 363–366. [CrossRef] [PubMed]
21. Dicken, M.J.; Aydin, K.; Pryce, I.M.; Sweatlock, L.A.; Boyd, E.M.; Walavalkar, S.; Ma, J.; Atwater, H.A. Frequency tunable near-infrared metamaterials based on VO_2 phase transition. *Opt. Express* **2009**, *17*, 18330–18339. [CrossRef] [PubMed]
22. Driscoll, T.; Kim, H.T.; Chae, B.G.; Di Ventra, M.; Basov, D.N. Phase-transition driven memristive system. *Appl. Phys. Lett.* **2009**, *95*, 043503. [CrossRef]
23. Kim, B.J.; Lee, Y.W.; Chae, B.G.; Yun, S.J.; Oh, S.Y.; Kim, H.T. Temperature dependence of the first-order metal-insulator transition in VO_2 and programmable critical temperature sensor. *Appl. Phys. Lett.* **2007**, *90*, 023515. [CrossRef]
24. Strelcov, E.; Lilach, Y.; Kolmakov, A. Gas sensor based on metal-insulator transition in VO_2 nanowire thermistor. *Nano Lett.* **2009**, *9*, 2322–2326. [CrossRef] [PubMed]
25. Heckman, E.M.; Gonzalez, L.P.; Guha, S.; Barnes, J.O.; Carpenter, A. Electrical and optical switching properties of ion implanted VO_2 thin films. *Thin Solid Films* **2009**, *518*, 265–268. [CrossRef]
26. Ureña-Begara, F.; Crunteanu, A.; Raskin, J.P. Raman and XPS characterization of vanadium oxide thin films with temperature. *Appl. Surf. Sci.* **2017**, *403*, 717–727. [CrossRef]
27. Chiu, T.W.; Tonooka, K.; Kikuchi, N. Growth of *b*-axis oriented VO_2 thin films on glass substrates using ZnO buffer layer. *Appl. Surf. Sci.* **2010**, *256*, 6834–6837. [CrossRef]
28. Zhang, P.; Jiang, K.; Deng, Q.; You, Q.; Zhang, J.; Wu, J.; Hu, Z.; Chu, J. Manipulations from oxygen partial pressure on the higher energy electronic transition and dielectric function of VO_2 films during a metal-insulator transition process. *J. Mater. Chem. C* **2015**, *3*, 5033–5040. [CrossRef]
29. Zhang, H.T.; Zhang, L.; Mukherjee, D.; Zheng, Y.X.; Haislmaier, R.C.; Alem, N.; Engel-Herbert, R. Wafer-scale growth of VO_2 thin films using a combinatorial approach. *Nat. Commun.* **2015**, *6*, 8475. [CrossRef] [PubMed]
30. Vernardou, D.; Pemble, M.E.; Sheel, D.W. The growth of thermochromic VO_2 films on glass by atmospheric-pressure CVD: A comparative study of precursors, CVD methodology, and substrates. *Chem. Vap. Depos.* **2006**, *12*, 263–274. [CrossRef]
31. Vernardou, D.; Paterakis, P.; Drosos, H.; Spanakis, E.; Povey, I.M.; Pemble, M.E.; Koudoumas, E.; Katsarakis, N. A study of the electrochemical performance of vanadium oxide thin films grown by atmospheric pressure chemical vapour deposition. *Sol. Energy Mater. Sol. Cells* **2011**, *95*, 2842–2847. [CrossRef]
32. Vernardou, D. Using an atmospheric pressure chemical vapor deposition process for the development of V_2O_5 as an electrochromic material. *Coatings* **2017**, *7*, 24. [CrossRef]
33. Makarevich, A.M.; Sadykov, I.I.; Sharovarov, D.I.; Amelichev, V.A.; Adamenkov, A.A.; Tsymbarenko, D.M.; Plokhih, A.V.; Esaulkov, M.N.; Solyankin, P.M.; Kaul, A.R. Chemical synthesis of high quality epitaxial vanadium dioxide films with sharp electrical and optical switch properties. *J. Mater. Chem. C* **2015**, *3*, 9197–9205. [CrossRef]
34. Blackburn, B.; Powell, M.J.; Knapp, C.E.; Bear, J.C.; Carmalt, C.J.; Parkin, I.P. $[\{VOCl_2(CH_2(COOEt)_2)\}_4]$ as a molecular precursor for thermochromic monoclinic VO_2 thin films and nanoparticles. *J. Mater. Chem. C* **2016**, *4*, 10453–10463. [CrossRef]
35. Rampelberg, G.; Schaekers, M.; Martens, K.; Xie, Q.; Deduytsche, D.; De Schutter, B.; Blasco, N.; Kittl, J.; Detavernier, C. Semiconductor-metal transition in thin VO_2 films grown by ozone based atomic layer deposition. *Appl. Phys. Lett.* **2011**, *98*, 162902. [CrossRef]
36. Premkumar, P.A.; Toeller, M.; Radu, I.P.; Adelmann, C.; Schaekers, M.; Meersschaut, J.; Conard, T.; Elshocht, S.V. Process study and characterization of VO_2 thin films synthesized by ALD using TEMAV and O_3 precursors. *ECS J. Solid State Sci. Technol.* **2012**, *1*, P169–P174. [CrossRef]
37. Tangirala, M.; Zhang, K.; Nminibapiel, D.; Pallem, V.; Dussarrat, C.; Cao, W.; Adam, T.N.; Johnson, C.S.; Elsayed-Ali, H.E.; Baumgart, H. Physical analysis of VO_2 films grown by atomic layer deposition and RF magnetron sputtering. *ECS J. Solid State Sci. Technol.* **2014**, *3*, N89–N94. [CrossRef]

38. Cerbu, F.; Chou, H.S.; Radu, I.P.; Martens, K.; Peter, A.P.; Afanas'ev, V.V.; Stesmans, A. Band alignment and effective work function of atomic-layer deposited VO_2 and V_2O_5 films on SiO_2 and Al_2O_3. *Phys. Status Solidi C* **2015**, *12*, 238–241. [CrossRef]
39. Zhang, K.; Tangirala, M.; Nminibapiel, D.; Cao, W.; Pallem, V.; Dussarrat, C.; Baumgart, H. Synthesis of VO_2 thin films by atomic layer deposition with TEMAV as precursor. *ECS Trans.* **2013**, *50*, 175–182. [CrossRef]
40. Blanquart, T.; Niinistö, J.; Gavagnin, M.; Longo, V.; Heikkilä, M.; Puukilainen, E.; Pallem, V.R.; Dussarrat, C.; Ritala, M.; Leskelä, M. Atomic layer deposition and characterization of vanadium oxide thin films. *RSC Adv.* **2013**, *3*, 1179–1185. [CrossRef]
41. Kozen, A.C.; Joress, H.; Currie, M.; Anderson, V.R.; Eddy, C.R., Jr.; Wheeler, V.D. Structural characterization of atomic layer deposited vanadium dioxide. *J. Phys. Chem. C* **2017**, *121*, 19341–19347. [CrossRef]
42. Park, H.H.; Larrabee, T.J.; Ruppalt, L.B.; Culbertson, J.C.; Prokes, S.M. Tunable electrical properties of vanadium oxide by hydrogen-plasma-treated atomic layer deposition. *ACS Omega* **2017**, *2*, 1259–1264. [CrossRef]
43. Musschoot, J.; Deduytsche, D.; Poelman, H.; Haemers, J.; Van Meirhaeghe, R.L.; Van den Berghe, S.; Detavernier, C. Comparison of thermal and plasma-enhanced ALD/CVD of vanadium pentoxide. *J. Electrochem. Soc.* **2009**, *156*, P122–P126. [CrossRef]
44. Boukhalfa, S.; Evanoff, K.; Yushin, G. Atomic layer deposition of vanadium oxide on carbon nanotubes for high-power supercapacitor electrodes. *Energy Environ. Sci.* **2012**, *5*, 6872–6879. [CrossRef]
45. Singh, T.; Wang, S.; Aslam, N.; Zhang, H.; Hoffmann-Eifert, S.; Mathur, S. Atomic layer deposition of transparent VO_x thin films for resistive switching applications. *Chem. Vap. Depos.* **2014**, *20*, 291–297. [CrossRef]
46. Daubert, J.S.; Lewis, N.P.; Gotsch, H.N.; Mundy, J.Z.; Monroe, D.N.; Dickey, E.C.; Losego, M.D.; Parsons, G.N. Effect of meso- and micro-porosity in carbon electrodes on atomic layer deposition of pseudocapacitive V_2O_5 for high performance supercapacitors. *Chem. Mater.* **2015**, *27*, 6524–6534. [CrossRef]
47. Baddour-Hadjean, R.; Golabkan, V.; Pereira-Ramos, J.P.; Mantoux, A.; Lincot, D. A Raman study of the lithium insertion process in vanadium pentoxide thin films deposited by atomic layer deposition. *J. Raman Spectrosc.* **2002**, *33*, 631–638. [CrossRef]
48. Badot, J.C.; Mantoux, A.; Baffier, N.; Dubrunfaut, O.; Lincot, D. Electrical properties of V_2O_5 thin films obtained by atomic layer deposition (ALD). *J. Mater. Chem.* **2004**, *14*, 3411–3415. [CrossRef]
49. Chen, X.; Pomerantseva, E.; Banerjee, P.; Gregorczyk, K.; Ghodssi, R.; Rubloff, G. Ozone-based atomic layer deposition of crystalline V_2O_5 films for high performance electrochemical energy storage. *Chem. Mater.* **2012**, *24*, 1255–1261. [CrossRef]
50. Badot, J.C.; Ribes, S.; Yousfi, E.B.; Vivier, V.; Pereira-Ramos, J.P.; Baffier, N.; Lincot, D. Atomic layer epitaxy of vanadium oxide thin films and electrochemical behavior in presence of lithium ions. *Electrochem. Solid-State Lett.* **2000**, *3*, 485–488. [CrossRef]
51. Kim, H.; Maeng, W.J. Applications of atomic layer deposition to nanofabrication and emerging nanodevices. *Thin Solid Films* **2009**, *517*, 2563–2580. [CrossRef]
52. George, S.M. Atomic layer deposition: An overview. *Chem. Rev.* **2010**, *110*, 111–131. [CrossRef] [PubMed]
53. Gelde, L.; Cuevas, A.L.; Martínez de Yuso, M.D.V.; Benavente, J.; Vega, V.; Gonzalez, A.S.; Prida, V.M.; Hernando, B. Influence of TiO_2-coating layer on nanoporous alumina membranes by ALD technique. *Coatings* **2018**, *8*, 60. [CrossRef]
54. Cheng, H.E.; Lee, W.J. Properties of TiN films grown by atomic-layer chemical vapor deposition with a modified gaseous-pulse sequence. *Mater. Chem. Phys.* **2006**, *97*, 315–320. [CrossRef]
55. Lee, W.J.; Hon, M.H. Space-limited crystal growth mechanism of TiO_2 films by atomic layer deposition. *J. Phys. Chem. C* **2010**, *114*, 6917–6921. [CrossRef]
56. Wu, C.; Zhang, X.; Dai, J.; Yang, J.; Wu, Z.; Wei, S.; Xie, Y. Direct hydrothermal synthesis of monoclinic VO_2(M) single-domain nanorods on large scale displaying magnetocaloric effect. *J. Mater. Chem.* **2011**, *21*, 4509–4517. [CrossRef]
57. Silversmit, G.; Depla, D.; Poelman, H.; Martin, G.B.; De Gryse, R. Determination of the V2p XPS binding energies for different vanadium oxidation states (V^{5+} to V^{0+}). *J. Electron. Spectrosc. Relat. Phenom.* **2004**, *135*, 167–175. [CrossRef]
58. Hryha, E.; Rutqvist, E.; Nyborg, L. Stoichiometric vanadium oxides studied by XPS. *Surf. Interface Anal.* **2012**, *44*, 1022–1025. [CrossRef]

59. Yuan, X.; Zhang, W.; Zhang, P. Hole-lattice coupling and photoinduced insulator-metal transition in VO_2. *Phys. Rev. B* **2013**, *88*, 035119. [CrossRef]
60. Zaghrioui, M.; Sakai, J.; Azhan, N.H.; Su, K.; Okimura, K. Polarized Raman scattering of large crystalline domains in VO_2 films on sapphire. *Vib. Spectrosc.* **2015**, *80*, 79–85. [CrossRef]
61. Shibuya, K.; Sawa, A. Polarized Raman scattering of epitaxial vanadium dioxide films with low-temperature monoclinic phase. *J. Appl. Phys.* **2017**, *122*, 015307. [CrossRef]

© 2018 by the authors. Licensee MDPI, Basel, Switzerland. This article is an open access article distributed under the terms and conditions of the Creative Commons Attribution (CC BY) license (http://creativecommons.org/licenses/by/4.0/).